Journal of Porous Materials (2022) 29:1039–1047
https://doi.org/10.1007/s10934-022-01227-z

Interzeolite conversion of HY to hierarchical HZSM-5 catalyst via an ionothermal route and its excellent catalytic performance in methanol-to-aromatics reaction

Zhigang Yang[1,2] · Yanru Li[1] · Dongliang Wang[1] · Xuefeng Long[1] · Hongwei Li[1] · Xinhong Zhao[1]

Accepted: 1 March 2022 / Published online: 18 March 2022

Abstract
Currently, synthesizing zeolites with specific physicochemical properties in a more environmentally benign and safe way is challenging. Herein we report a novel ionothermal route of preparing HZSM-5 zeolite, which is featured by the direct interzeolite transformation of HY to HZSM-5. The appropriate synthetic conditions of this HZSM-5 material are refined. Although performing a series of optimization, the resultant product still contains minor $(NH_4)_3AlF_6$ impurity. Pure HZSM-5 phase with high relative crystallinity can be obtained through successive calcination and acid-washing treatments towards the as-made sample. SEM–EDS characterization and nitrogen physisorption measurement reveal that this pure HZSM-5 sample is composed of classical coffin-like crystals with a low Si/Al ratio and evident hierarchical micro-mesoporous structure. Benefiting from its unique physicochemical properties, this pure HZSM-5 catalyst exhibits more superior methanol-to-aromatics performance than those of the state-of-the-art HZSM-5 and Metal/ZSM-5 catalysts evaluated under similar reaction conditions. It can be anticipated that this HZSM-5 material may be applied in other industrially relevant reactions owing to its particular structure and properties.

Keywords HZSM-5 · HY · Ionothermal synthesis · Methanol-to-aromatics reaction · Interzeolite conversion

1 Introduction

As a class of versatile materials, zeolites have been extensively used in the fields of adsorption separation, ion exchange, and catalytic process due to their unique pore architecture, high surface area, and specific acidity [1, 2]. Among the diverse research fields of zeolite science and technology, the synthesis chemistry of zeolite materials is perhaps the most fascinating. Except for conventional hydrothermal synthesis, a series of intriguing nonconventional synthesis methodologies of zeolites were successively fabricated in the past several decades, such as solvothermal/ionothermal synthesis [3, 4], OSDA/solvent-free synthesis (OSDA: Organic Structure-Directing Agent) [5, 6], interzeolite conversion (IZC) [7], charge density mismatch [8], free-radical-assisted synthesis [9], continuous flow synthesis [10], microwave/ultrasound-assisted synthesis [11, 12], topotactic transformation [13] and ADOR route [14]. Historically, these novel methods played extremely crucial roles in obtaining the zeolite materials with new topologies and compositions. Among these, IZC is quite attractive one. The main advantage of IZC is that it allows the more selective and rapid synthesis of certain valuable zeolite topologies with particular physicochemical properties.

Among 255 different zeolite topologies approved by the International Zeolite Association till now, Y and ZSM-5 zeolites are perhaps the most valuable and well-studied commercial zeolite catalysts. USY zeolite is the backbone of fluid catalytic cracking process (FCC), while ZSM-5 is the second widely used component [15]. Recently, the interzeolite conversion of the two zeolite materials, that is Y zeolite to ZSM-5, received considerable attention. One of the main benefits of this process is that it can reutilize the spent FCC catalysts that are massively produced in the oil refining. Goel et al. [16] obtained high-silica ZSM-5 from Y zeolite in the presence of seeds using OSDA-free

✉ Xinhong Zhao
licpzhaoxh@lut.edu.cn

[1] School of Petrochemical Technology, Lanzhou University of Technology, Lanzhou 730050, China

[2] Gansu Chemical Industry Research Institute Co., Ltd., Lanzhou 730020, Gansu, China

interzeolite transformation method. Rimer's group and Mascarenhas et al. found that this process can be achieved in the absence of OSDA and seeds [17, 18]. Goel et al. [19] achieved the encapsulation of metal clusters within ZSM-5 via interzeolite transformations assisted by ZSM-5 seeds or organic templates. Despite great success in this direction, it should be mentioned that the above interzeolite conversions were exclusively carried out under hydrothermal conditions. It is well known that large amounts of wastes and high autogenous pressure will be inevitably produced during this hydrothermal conversion process. These disadvantages, on the one hand, bring about some environmental and safety issues, on the other hand, cause great difficulty in exploring the formation mechanism of zeolites with conventional techniques due to the presence of high pressure. From this point of view, developing a new and more sustainable interzeolite conversion route to obtain targeted zeolite topology with ideal physicochemical properties is highly desirable.

Ionothermal and solvent-free synthesis recently attracted extensive interest, for the two particular synthetic methods of zeolites could be conducted at ambient pressure. Benefiting from this feature, Tian's group could successfully use multinuclear solid-state NMR technique to study the formation mechanism of aluminophosphate molecular sieves by ionothermal method [20]. Very recently, Xiao's group reported the generalized ionothermal synthesis of silica-based zeolites that was once considered as a big challenge [21]. Meantime, the combination of IZC with solvent-free synthesis has achieved great success. Xiong et al. reported the rapid interzeolite transformation of Y into SSZ-13 in the absence of water [22]. Miyagawa et al. successfully prepared SSZ-13 zeolite via the interzeolite transformation route under solvent/OSDA-free conditions [23]. Xu et al. reported the solvent-free interzeolite conversion of Y to SSZ-39 in the presence of OSDA and zeolite seeds [24]. To the best of our knowledge, the interzeolite conversion of Y to ZSM-5 under ionothermal (or solvent-free) conditions has not yet been reported by any researchers until now.

Benzene, toluene, and xylene (BTX) are the most crucial bulk raw materials for producing various high-value-added chemicals. Traditionally, BTX is produced by catalytic reforming and cracking of petroleum [25]. However, for those districts poor in petroleum resources but rich in coal, these traditional routes of producing BTX are not cost-effective. As an ideal alternative, methanol-to-aromatics reaction (MTA) recently received extensive interest around the world because methanol is readily available from various carbon resources, including coal and natural gas [26]. HZSM-5 is perhaps the most widely-used catalyst in the MTA reaction owing to its unique pore architecture and properties. Although great progress has been made in this field, this process still suffered from poor catalytic stability and BTX selectivity [27, 28].

Inspired by the above-mentioned Xiao's work [21], herein we attempted to conduct the interzeolite conversion of HY zeolite to HZSM-5 by a novel ionothermal route. The purposes of our work are to strengthen our understanding on the synthesis chemistry of IZC and meantime obtain HZSM-5 catalysts with particular properties different from those by other routes. To this end, the major factors influencing this process, such as the mass ratios of NH_4F/HY and TPABr/HY (TPABr:tetrapropylammonium bromide), crystallization temperature, and time, were thoroughly investigated. The resultant HZSM-5 zeolite with good crystallinity was selected and characterized by various techniques, and its catalytic performance was evaluated in the methanol-to-aromatics (MTA) reaction.

2 Experimental section

2.1 Materials

HY zeolite ($SiO_2/Al_2O_3 = 11.5$, Tianjin Nanhua Catalyst Co., Ltd.), HZSM-5 ($SiO_2/Al_2O_3 = 300$, Tianjin Nanhua Catalyst Co., Ltd.), 1-ethyl-3-methyl imidazolium bromide (denoted as ILs, 98 wt.%, Meryer (Shanghai) Chemical Technology Co., Ltd.), ammonium fluoride (98 wt.%, Meryer (Shanghai) Chemical Technology Co., Ltd.), tetrapropylammonium bromide (denoted as TPABr, 98 wt.%, Aladdin Reagent), nitric acid (65–68 wt.% in water, Sinopharm Chemical Reagent Co. Ltd), methanol (AR, 99.7 wt.%, Sinopharm Chemical Reagent Co. Ltd), deionized water (homemade).

2.2 Synthesis of HZSM-5 from zeolite HY

The process of preparing HZSM-5 zeolite: HY zeolite (0.80 g), NH_4F, TPABr, ZSM-5 seed crystals, 1-ethyl-3-methyl imidazolium bromide (ILs), and deionized water were measured out and added into a mortar in turn according to the following mass ratio of HY: NH_4F: TPABr: Seeds: ILs: $H_2O = 1$: (0–1.88):(0–0.57):0.025:6.25:0.38. Then the starting materials were mixed and ground by a pestle for 20 min. The milled precursor mixture was transferred to a 50 mL Teflon-lined autoclave and crystallized at 160–200 °C for 24–96 h. Finally, the crystallized samples were collected, washed with deionized water, and dried at 120 °C for 2–3 h in air atmosphere. The as-made solid samples were calcined at 550 °C for 4 h to remove the template. The detailed synthesis conditions were summarized in Table1.

To obtain pure HZSM-5 sample, the above-calcined product was treated with 1 M HNO_3 solution at 70 °C for 6 h. Then the product was washed with deionized water and ethanol by centrifugation until the supernatant was neutral. The washed product was dried at 120 °C for 2 ~ 3 h to obtain HZSM-5 zeolite catalyst.

Table 1 The sample names, initial composition, crystallization conditions and the product phase

Samples	HY:NH_4F:TPABr: seed:ILs:H_2O (mass ratio)	Time (h)	Tem (°C)	Product phase
NH_4F-0	1.00: **0**: 0.38: 0.025: 6.25:0.38	96	180	HY
NH_4F-0.63	1.00:**0.63**:0.38:0.025:6.25:0.38	96	180	$(NH_4)_3AlF_6$
NH_4F-1.25	1.00:**1.25**:0.38:0.025:6.25:0.38	96	180	HZSM-5 + $(NH_4)_3AlF_6$
NH_4F-1.88	1.00:**1.88**:0.38:0.025:6.25:0.38	96	180	HZSM-5 + $(NH_4)_3AlF_6$
TPABr-0	1.00:1.25: **0**: 0.025: 6.25:0.38	96	180	$(NH_4)_3AlF_6$
TPABr-0.19	1.00:1.25:**0.19**:0.025:6.25:0.38	96	180	$(NH_4)_3AlF_6$
TPABr-0.57	1.00:1.25:**0.57**:0.025:6.25:0.38	96	180	HZSM-5 + $(NH_4)_3AlF_6$
T160t96	1.00:1.25:0.38:0.025:6.25:0.38	**96**	**160**	HZSM-5 + $(NH_4)_3AlF_6$
T200t96	1.00:1.25:0.38:0.025:6.25:0.38	**96**	**200**	$(NH_4)_3AlF_6$
T180t24	1.00:1.25:0.38:0.025:6.25:0.38	**24**	**180**	$(NH_4)_3AlF_6$
T180t48	1.00:1.25:0.38:0.025:6.25:0.38	**48**	**180**	$(NH_4)_3AlF_6$
T180t72	1.00:1.25:0.38:0.025:6.25:0.38	**72**	**180**	$(NH_4)_3AlF_6$
NH_4F-1.25-C[a]	–	–	–	HZSM-5 + amorphous
NH_4F-1.25-C-AT[b]	–	–	–	HZSM-5

[a]The sample NH_4F-1.25-C is the calcined version of the as-synthesized sample NH_4F-1.25

[b]The sample NH_4F-1.25-C-AT is the acid-treatment version of the sample NH_4F-1.25-C

2.3 Characterizations

Powder X-Ray diffraction (XRD) patterns of the products were conducted on a D/Max-2400 Rigaku diffractometer under the conditions of Cu K_α radiation, 40 kV, 150 mA, and a scan speed of 1.2° (2θ) min^{-1}. Scanning electron microscope images were obtained from an SEM (TESCAN MIRA3) instrument. Energy disperse spectroscopy (EDS) were obtained from a JEOL JEM-2010 instrument. Nitrogen physisorption measurements were carried out on a Micromeritics ASAP 2020 adsorption instrument at − 196 °C. Samples were degassed at 150 °C for 4 h before the measurements. Specific surface areas of zeolite materials were calculated from the adsorption data obtained at P/P_0 between 0.06 and 0.20, using the Brunauer–Emmett–Teller (BET) equation. The micropore volumes were determined by the t-plot method. The adsorption branch data were used to plot the pore size distribution curve.

2.4 Catalytic reaction

The methanol to aromatics reaction (MTA) was performed on a fixed-bed flow reactor (Boya Automation Equipment Co. Ltd) at atmospheric pressure. Typically, 0.5 g of HZSM-5 catalyst diluted with quartz sand was loaded in the reactor with 700 mm length and 10 mm inner diameter, which was pretreated at 400 °C in N_2 flow of 20 mL/min for 1 h. Before methanol entered the reactor, it was firstly vaporized in the gasification chamber and then mixed with N_2 into the reactor at the weighted hourly space velocity (WHSV) of 1.9 h^{-1}. The effluent products were analyzed by an online gas chromatograph (Tianmei GC-7890II, Shanghai), which was equipped with a flame ionization detector (FID) and a SE-30 capillary column.

3 Results and discussion

3.1 Optimization of the interzeolite conversion conditions

In the present research, a series of experiments were carried out to explore the effects of NH_4F/HY ratio, TPABr/HY ratio, crystallization temperature, and time on the interzeolite conversion of HY to HZSM-5 zeolite. The initial mass ratio of starting materials, that is, HY:NH_4F:TPABr:Seeds:ILs:H_2O = 1:(0–1.88):(0–0.57):0.025:6.25:0.38, was attempted to conduct this conversion. It was reported in the literature that the molar ratio of OH^-/SiO_2 and Na^+/SiO_2 must be strictly controlled during the hydrothermal conversion of Y zeolite to ZSM-5 [18]. This indicates that the reaction conditions have a significant impact on the final product phase. Thus, it is essential to investigate the various factors that influence the conversion of HY to HZSM-5 under ionothermal conditions.

3.1.1 The effect of NH_4F/HY mass ratio

The effect of NH_4F/HY ratio on the interzeolite conversion of HY to HZSM-5 zeolite is shown in Fig. 1. As shown in Fig. 1, when no NH_4F is added to the precursor mixture, the product phase in the sample NH_4F-0 is HY zeolite with FAU topology, i.e., the starting material. When the NH_4F/HY ratio is increased to 0.63, the main

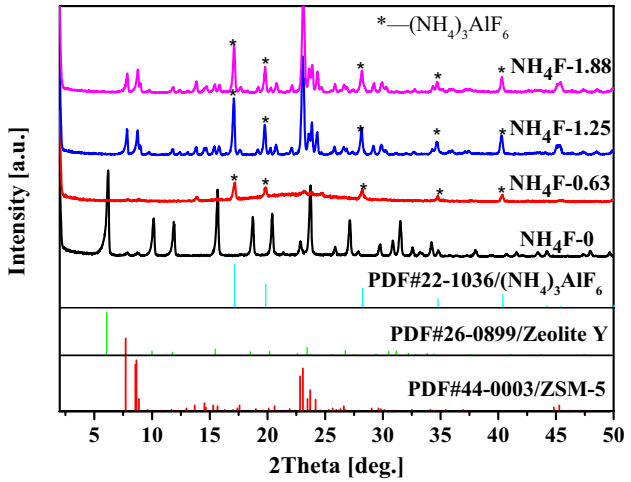

Fig.1 XRD patterns of products synthesized under the conditions of different mass ratio of NH_4F/HY, together with those of $(NH_4)_3AlF_6$ and Y and ZSM-5 as the references

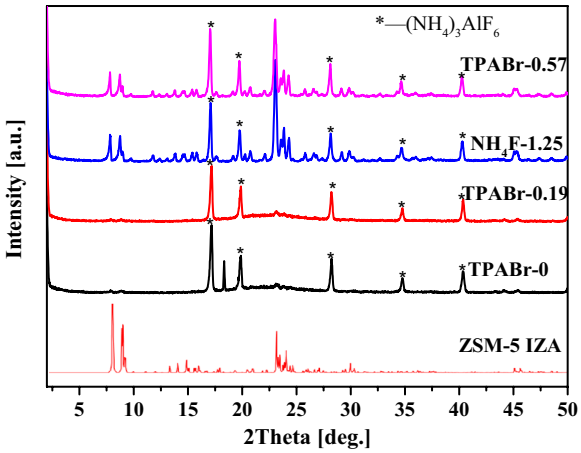

Fig. 2 XRD patterns of products synthesized under the conditions of different TPABr/HY mass ratio. For the sample NH_4F-1.25, the ratio is 0.38

product phase observed in the sample NH_4F-0.63 becomes $(NH_4)_3AlF_6$ compound. These results indicate that only when NH_4F is introduced to the synthesis system can the initial HY zeolite be disassembled into locally ordered aluminosilicate species (nanoparts) [29] or ring building units (RBU) [18]. It is well known that fluoride ions as a mineralizing agent can help to dissolve silica or other T-atoms sources by chelation or coordination for the zeolite synthesis [30]. The introduction of fluoride ions allows the crystallization of zeolite under nearly neutral or acidic conditions, as compared to the typical zeolite synthesis in hydroxide solution. Since our synthesis system is in a more acidic environment, ammonium fluoride may be an indispensable agent for the interzeolite conversion of HY to HZSM-5. In particular, when the NH_4F/HY ratio is higher than 0.63 (samples NH_4F-1.25, NH_4F-1.88), the primary product phase is HZSM-5, but accompanied by evident $(NH_4)_3AlF_6$ impurity phase. This result indicates that the crystal structure of the starting HY zeolite will be completely destroyed under a high NH_4F/HY mass ratio, meanwhile the nucleation and growth of the new zeolite phase (HZSM-5 zeolite) is taking place under the ionothermal conditions. This finding is consistent with the opinion proposed by Xiao's group, who considered that the successful synthesis of silica-based zeolites by the ionothermal method strongly relied on the introduction of an appropriate amount of NH_4F [21]. On the other hand, the appearance of $(NH_4)_3AlF_6$ implied that the degradation of HY may initiate from the extraction of the aluminum atoms by NH_4F. In the latest review by Dusselier's group, the critical role of aluminum was discussed and identified during the interzeolite conversion synthesis [31].

3.1.2 The effect of TPABr/HY mass ratio

The influence of TPABr/HY ratio on the transformation of HY was investigated here, since the quaternary ammonium salt TPABr is a commonly used OSDA for the synthesis of ZSM-5 zeolite catalyst [32–34] and the main synthesis cost is related to the use of expensive OSDA. As shown in Fig. 2, only $(NH_4)_3AlF_6$ impurity phase is formed when the TPABr/HY ratio is in the range of 0–0.19 (samples TPABr-0, TPABr-0.19). When the mass ratio of TPABr/HY is not lower than 0.38 (samples NH_4F-1.25, TPABr-0.57), HZSM-5 zeolite phase appears, but $(NH_4)_3AlF_6$ impurity phase can also be detected in the two samples. These results suggest that the nanoparts (or RBU) from the disassembly of HY zeolite cannot be reassembled into HZSM-5 zeolite in the absence of a suitable amount of TPABr [29]. In this study, the appropriate mass ratio of TPABr/HY should be not less than 0.38.

3.1.3 The effect of crystallization temperature

It is generally accepted that the structure of zeolites generated from the synthesis system strongly relies on the crystallization temperature [35]. Here, three crystallization temperatures of 160 °C, 180 °C, and 200 °C, of which 180 °C is the frequently employed one in the hydrothermal synthesis of ZSM-5 zeolite, were investigated in the present interzeolite conversion process, and its effect on the resulting product phase was studied in detail using XRD technique. As shown in Fig. 3, when the conversion process is performed at 200 °C (sample T200t96), only the complex $(NH_4)_3AlF_6$ is obtained with no observable HZSM-5 phase. This result may relate to the Hoffman degradation of TPABr caused by high temperature [36]. In particular, when the crystallization

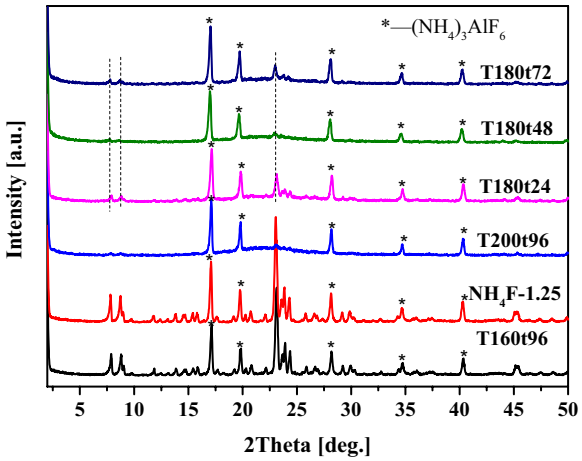

Fig. 3 XRD patterns of products synthesized under different crystallization temperature and time. For the sample NH_4F-1.25, its crystallization conditions are 180 °C and 96 h

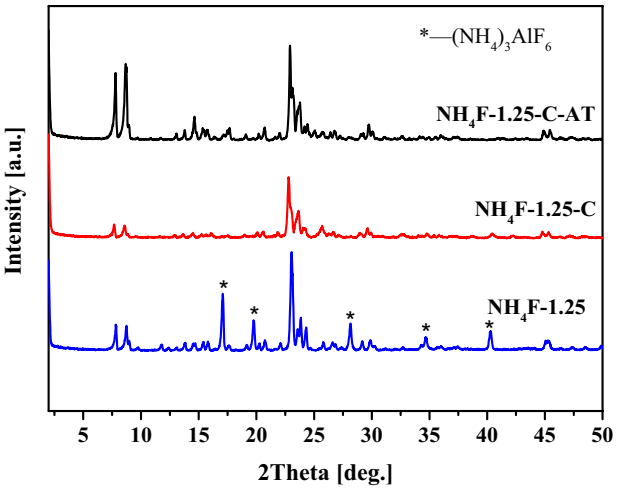

Fig.4 XRD patterns of the samples subjected to calcination and acid –washing treatments. For the two samples NH_4F-1.25-C and NH_4F-1.25-C-AT, the symbols "C" and "AT" after the number 1.25 represent calcination and acid-washing treatment, respectively

temperature is not higher than 180 °C (samples NH_4F-1.25 and T160t96), this conversion process can be successfully accomplished. Nevertheless, the impurity phase $(NH_4)_3AlF_6$ is still detected in the final products. As a comparison, the diffraction peak intensity of HZSM-5 phase in the sample NH_4F-1.25 is slightly higher than that of the sample at 160 °C. This may be due to the fact that the higher temperature is conducive to the interaction of the reaction mixture, thereby reducing the need for nucleation [32]. Obviously, the suitable temperature range is 160–180 °C for the interzeolite conversion of HY to HZSM-5 under ionothermal conditions.

3.1.4 The effect of crystallization time

To understand the transformation process of HY zeolite to HZSM-5, the duration of 24 h, 48 h, 72 h, and 96 h was studied in detail and the XRD patterns of the resultant products are also shown in Fig. 3. For the three samples (T180t24, T180t48, T180t72) synthesized in the period of 24–72 h, it can be seen from their XRD patterns that three faint characteristic peaks attributed to HZSM-5 can be clearly observed at $2\theta = 7.9°$, 8.8°, and 23.3°. In contrast, the characteristic peaks of HY zeolite are not detected throughout this stage. This result indicates that the parent HY zeolite is completely dissolved and its conversion to HZSM-5 has initiated when the crystallization time reaches 24 h, verifying the remarkable efficiency of the phase transition between zeolites. The nanoparts (or RBU) from the dissolution process will be rebuilt under the action of the OSDA to form MFI topological structure of HZSM-5 zeolite [37]. It is worthwhile to note that the three weak diffraction peaks relevant to HZSM-5 zeolite almost do not increase in intensity with the prolonging crystallization time during the period of 24–72 h. This result implies that this stage may be considered as the induction period (or the nucleation period). It should be noted that the characteristic diffraction peaks corresponding to the MFI structure become apparent when the duration is extended from 72 to 96 h (sample NH_4F-1.25), indicating that the crystal growth may undergo an abrupt acceleration during this period. According to the previous research [30], it is reasonable to assume that the HZSM-5 zeolite crystals crystallized in the presence of fluoride media may become more perfect and contain fewer defect sites with the extended crystallization time. This should also be responsible for the observed enhanced diffraction peak intensity. Moreover, one can see that the diffraction peaks of $(NH_4)_3AlF_6$ complex do not exhibit an evident change in intensity during the entire crystallization period investigated here. This result manifests that $(NH_4)_3AlF_6$ may not serve as the nutrients of forming the HZSM-5 zeolite. Based on the above discussions, it is easily seen that the suitable crystallization time should be not less than 96 h for the interzeolite conversion of HY to HZSM-5.

3.1.5 The effects of calcination and acid treatment on the product phase

Although performing a series of optimization experiments, the complex $(NH_4)_3AlF_6$ impurity phase invariably exists in the resultant products. To eliminate it from the product, high-temperature calcination and acid-washing experiments were successively conducted to process the as-synthesized sample. As shown in Fig. 4, no diffraction lines assigned to the complex $(NH_4)_3AlF_6$ impurity phase could be observed in the XRD pattern of the sample NH_4F-1.25-C after the as-made sample NH_4F-1.25 was subjected to the calcination

treatment. This implies that the impurity phase may undergo decomposition and become amorphous materials that cannot be detected by XRD. It should be noted that the characteristic diffraction peak intensity of the ZSM-5 zeolite decreases slightly after this calcination treatment. This may be attributed to the coverage of HZSM-5 zeolite crystals by amorphous aluminum species (denoted as AAS) from the decomposition of $(NH_4)_3AlF_6$. After the sample NH_4F-1.25-C is further treated with 1.0 M HNO_3, the characteristic peaks corresponding to the MFI structure increase significantly in intensity, as can be seen from the XRD pattern of the sample NH_4F-1.25-C-AT. This result suggests that the relative crystallinity of HZSM-5 zeolite is evidently improved after this acid-washing treatment. This observed high crystallinity may be, on the one hand, relevant to the elimination of those unwanted AAS, on the other hand, to the removal of extra-framework aluminum species occluded in the micropores. Obviously, the successive calcination and acid-washing treatments significantly improve the quality of this HZSM-5 material, which makes it a promising catalyst in many industrial applications.

3.2 Morphology and pore structure analysis of HZSM-5 zeolite

The SEM and EDS images of the samples NH_4F-1.25-C and NH_4F-1.25-C-AT are shown in Fig. 5. The sample NH_4F-1.25-C is mainly composed of coffin-like crystals and some flocculent matter, of which the former morphology is very typical for ZSM-5 zeolite and its crystal size is about 5 μm (Fig. 5a). From the corresponding EDS mapping profile (Fig. 5c) of this sample, it can be seen that the flocculent matter is of an aluminum-rich material, which strongly indicates that it should originate from the decomposition of the complex $(NH_4)_3AlF_6$ impurity phase. As a contrast, the sample NH_4F-1.25-C-AT resembled as the sample 1.0-NH_4F-C in terms of the morphology and crystal size of HZSM-5 zeolite (Fig. 5b). It should be mentioned that the flocculent matter that appeared in the sample NH_4F-1.25-C cannot be observed in the SEM micrograph of the sample NH_4F-1.25-C-AT. These results reveal that this mild acid treatment can effectively get rid of the flocculent matter, meanwhile not prominently impair the crystal structure of HZSM-5 zeolite. The Si/Al ratio of the sample NH_4F-1.25-C-AT determined by EDS (Fig. 5d) is about 21, slightly higher than that of the parent HY zeolite. This result unambiguously proves the previous speculation that some specific aluminum species from HY zeolite must coordinate with NH_4F to form the complex $(NH_4)_3AlF_6$.

Figure 6A shows the N_2 adsorption/desorption isotherms of the representative samples NH_4F-1.25-C and NH_4F-1.25-C-AT. It can be seen from the figure that both samples exhibit a higher N_2 adsorption capacity at the low relative pressure zone ($P/P_0 < 0.01$), indicating that they have a typical microporous structure. In addition, both samples show an evident nitrogen uptake at the pressure zone of $0.1 < P/P_0 < 0.2$, suggesting that the two samples contain narrow mesopores. The pore size distribution curves shown in Fig. 6B also support this speculation. From this figure, it can be found that the mesopore size of the two samples is centered at 1.9–2.3 nm. As can be seen from the SEM images (Fig. 5), no apparent intercrystalline void can be observed for the samples, which strongly implies that these mesopores must result from the intracrystalline void. According to the reference [38], the formation of these intracrystalline mesopores should be a natural result caused by the increase of crystal phase density during the

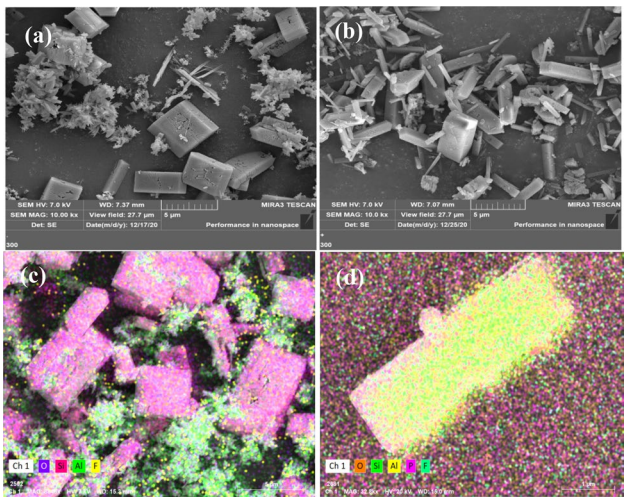

Fig.5 SEM and EDS-mapping images of two representative HZSM-5 samples (**a**, **c**): NH_4F-1.25-C; (**b**, **d**): NH_4F-1.25-C-AT

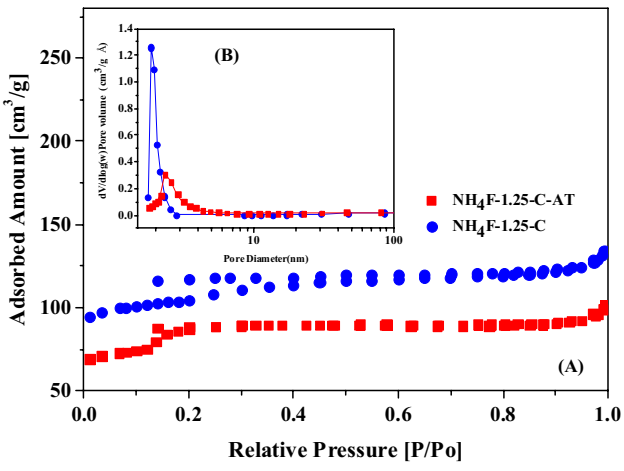

Fig.6 N_2 adsorption/desorption isotherms (**A**) and pore size distribution curves (**B**) of two representative HZSM-5 samples

interzeolite conversion of HY zeolite (FD: 12.7 T/1000 Å^3) to HZSM-5 (FD: 17.9 T/1000 Å^3). It is well known that the introduction of mesopores in the microporous zeolite materials can effectively promote the diffusion of bulky molecules, thereby reducing their diffusion limitation [39–41]. On the other hand, these mesopores in zeolite catalysts also provide enough space to accommodate the carbon deposition species generated by the reaction, thereby inhibiting the micropores blocking by carbon deposition to a certain extent [42].

As can be seen from Table 2, the sample NH_4F-1.25-C-AT exhibits a much higher microporous surface area (204 m^2/g vs. 70 m^2/g) and microporous volume (0.096 cm^3/g vs. 0.026 cm^3/g), comparable BET surface area (299 m^2/g vs. 314 m^2/g), and mesoporous volume (0.085 cm^3/g vs. 0.098 cm^3/g) when compared to the sample NH_4F-1.25-C. For the sample NH_4F-1.25-C-AT, its enhanced microporous parameters should be attributed to the removal of amorphous-like materials occluded in the micropores of the sample NH_4F-1.25-C. However, in comparison to data in the literature [43–46], the microporous parameters of the sample NH_4F-1.25-C-AT are still relatively low. Nevertheless, this sample may have a high potential in the petrochemical field due to the presence of unobstructed micropores and evident intracrystalline mesopores.

3.3 MTA catalytic performance

Figure 7 shows the BTX's and aromatics' selectivity versus time-on-stream in the methanol-to-aromatics reaction over the NH_4F-1.25-C-AT catalyst. The methanol conversion (not shown) is invariably larger than 95% during the period of 5–160 h. As shown in the figure, the BTX's and aromatics' selectivity gradually increase to 43% and 54%, respectively, within the initial reaction time of 10 h. They fall in the range of 35.0–46.6% and 50–62% respectively during the period of 10–160 h. Even after 160 h reaction, the BTX's and aromatics' selectivity do not decline sharply. It can be seen from Table 2 and Fig. 7 that the overall catalytic performance of this NH_4F-1.25-C-AT catalyst is superior to those of the

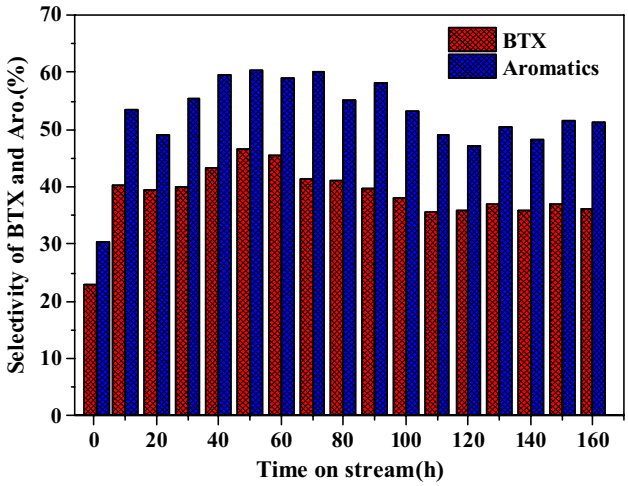

Fig. 7 Evolution of BTX's and aromatics' selectivity versus time-on-stream in the methanol-to-aromatics reaction over the NH_4F-1.25-C-AT catalyst. Reaction conditions: 400 °C, 0.1 MPa, WHSV = 1.9 h^{-1}

state-of-the-art HZSM-5 and Metal/ZSM-5 catalysts [43–45]. As indicated in the literature, BTX selectivity would continue to decrease at the beginning of the reaction. When the reaction time reached 60 h, the BTX selectivity would drop to less than 35%. For this NH_4F-1.25-C-AT catalyst, its excellent catalytic performance, especially its high BTX selectivity and long catalytic lifetime, should be attributed to the following several factors. Firstly, the presence of naturally produced mesopores in our HZSM-5 catalyst will substantially reduce the mass transfer limitations of bulky molecules. Secondly, it was reported by Flaherty's group that the suitable ratio of HF/TPA would reduce or completely eliminate the silanol defects in the MFI structure [47]. It has been recognized that the presence of silanol defects will lead to the problem of catalyst deactivation as they are inclined to trap heavy hydrocarbons (i.e., carbon) [48]. Finally, all aluminum atoms prefer to be located at the intersections of straight and sinusoidal channels of HZSM-5 due to the sole use of bulky OSDA molecules

Table 2 Textural parameters of two representative samples and the catalytic performance in MTA reaction

Catalysts[a]	S_{BET}/(m^2/g)	S_{Micro}/(m^2/g)	S_{Exter}/(m^2/g)	V_{Micro}/(cm^3/g)	V_{Meso}/ (cm^3/g)	Sel. $_{BTX}$ (%)	Lifetime (h)
NH_4F-1.25-C	314	70	244	0.026	0.098	n.a	n.a
NH_4F-1.25-C-AT	299	204	95	0.096	0.085	35.0–46.6	> 160
NSHZ	429	323	106	0.14	0.13	36.56	< 110[44]
D-HZSM-5–12	385	333	42	0.129	0.146	34.05	< 80[45]
NZ3	398	241	157	0.10	0.13	48.27	< 175[46]
Nano-ZSM-5	379	266	113	0.08	0.26	34.2	n.a [47]

[a]Reaction conditions: NSHZ (400 °C, 0.1 MPa, WHSV = 1.2 h^{-1}); D-HZSM-5–12(400 °C, 0.1 MPa, WHSV = 1 h^{-1}); NZ3 (400 °C, 0.1 MPa, WHSV = 0.8 h^{-1}); Nano-ZSM-5 (370 °C, 0.1 MPa, WHSV = 2.6 h^{-1})

(i.e., TPABr) [49, 50]. This siting of Al atoms would bring about a remarkable impact on this MTA reaction. Future study to fully explore the potential of this HZSM-5 catalyst is still underway in our lab.

4 Conclusions

In this work, a novel ionothermal route is successfully developed to perform the interzeolite conversion of HY to HZSM-5. The suitable initial composition for this HZSM-5 material is HY: NH_4F: TPABr: Seeds: ILs: H_2O = 1:1.25:0.38:0.025:6.25:0.38 (mass ratio). The minor $(NH_4)_3AlF_6$ impurity phase in the resulting representative sample can be eliminated by successive calcination and acid-washing treatments to obtain pure HZSM-5 zeolite with high relative crystallinity. Owing to its low Si/Al ratio and unique hierarchical micro-mesoporous structure, this HZSM-5 catalyst exhibits excellent catalytic performance in the methanol-to-aromatics reaction (MTA), giving methanol conversion of higher than 95% and BTX selectivity of 35.0–46.6%, with a lifetime longer than 160 h. This newly developed synthetic route may throw light on the preparation of other zeolite catalysts with more superior catalytic performance in the MTA reaction.

Acknowledgements This work was supported by the National Natural Science Foundation of China (Grant No. 21666019, 22168022) and The Youth Natural Science Foundation of Gansu Province (Grant No. 20JR10RA189). We cordially thank the Reviewers and Editors for providing us with valuable comments and suggestions.

Author contributions Mr. ZY wrote the original draft. Ms. YL conducted the material syntheses. Dr. DW analyzed the XRD data. Dr. XL conducted the SEM analysis. Dr. HL measured the catalytic performance. Prof. XZ proposed the project and revised the draft.

Funding See Acknowledgements part.

Data availability The datasets generated during and/or analysed during the current study are available from the corresponding author on reasonable request.

Code availability Not Applicable.

Declarations

Conflict of interest The authors declare that they have no known competing financial interests or personal relationships that could have appeared to influence the work reported in this paper.

References

1. P. del Campo, C. Martinez, A. Corma, Chem. Soc. Rev. **50**, 8511–8595 (2021)
2. M. Dusselier, M.E. Davis, Chem. Rev. **118**, 5265–5329 (2018)
3. E.R. Cooper, C.D. Andrews, P.S. Wheatley, P.B. Webb, P. Wormald, R.E. Morris, Nature **430**, 1012–1016 (2004)
4. Q.S. Huo, R.R. Xu, J. Chem. Soc.-Chem. Commun. (1992). https://doi.org/10.1039/c39920000168
5. N. Eng-Poh, D. Chateigner, T. Bein, V. Valtchev, S. Mintova, Science **335**, 70–73 (2012)
6. L. Ren, Q. Wu, C. Yang, L. Zhu, C. Li, P. Zhang, H. Zhang, X. Meng, F.-S. Xiao, J. Am. Chem. Soc. **134**, 15173–15176 (2012)
7. R.M. Barrer, J. Chem. Soc. **2**, 127–132 (1948)
8. Lewis GJ, Miller MA, Moscoso JG, Wilson BA, Knight LM, Wilson ST in: Studies in Surface Science and Catalysis, Vol. 154, eds. E. van Steen, I.M. Claeys and L.H. Callanan (Elsevier, 2004).
9. G. Feng, P. Cheng, W. Yan, M. Boronat, X. Li, J.-H. Su, J. Wang, Y. Li, A. Corma, R. Xu, J. Yu, Science **351**, 1188–1191 (2016)
10. Z.D. Liu, T. Wakihara, K. Oshima, D. Nishioka, Y. Hotta, S.P. Elangovan, Y. Yanaba, T. Yoshikawa, W. Chaikittisilp, T. Matsuo, T. Takewaki, T. Okubo, Angew. Chem.-Int. Ed. **54**, 5683–5687 (2015)
11. P. Chu, F.G. Dwyer, J.C. Vartuli, *Crystallization method employing microwave radiation* (Mobil Oil Corporation (New York, NY), United States, 1988)
12. Ö. Andaç, M. Tatlıer, A. Sirkecioğlu, I. Ece, A. Erdem-Şenatalar, Microporous Mesoporous Mater. **79**, 225–233 (2005)
13. W.J. Roth, P. Nachtigall, R.E. Morris, P.S. Wheatley, V.R. Seymour, S.E. Ashbrook, P. Chlubná, L. Grajciar, M. Položij, A. Zukal, O. Shvets, J. Čejka, Nat. Chem. **5**, 628–633 (2013)
14. M. Mazur, P.S. Wheatley, M. Navarro, W.J. Roth, M. Položij, A. Mayoral, P. Eliášová, P. Nachtigall, J. Čejka, R.E. Morris, Nat. Chem. **8**, 58–62 (2016)
15. M.A. Alabdullah, A.R. Gomez, J. Vittenet, A. Bendjeriou-Sedjerari, W. Xu, I.A. Abba, J. Gascon, ACS Catal. **10**, 8131–8140 (2020)
16. S. Goel, S.I. Zones, E. Iglesia, Chem. Mater. **27**, 2056–2066 (2015)
17. W. Qin, R. Jain, F.C. Robles Hernández, J.D. Rimer, Chem. A—Eur. J. **25**, 5893–5898 (2019)
18. M.B. dos Santos, K.C. Vianna, H.O. Pastore, H.M.C. Andrade, A.J.S. Mascarenhas, Microporous Mesoporous Mater. **306**, 110413 (2020)
19. S. Goel, S.I. Zones, E. Iglesia, J. Am. Chem. Soc. **136**, 15280–15290 (2014)
20. R. Xu, W. Zhang, J. Xu, Z. Tian, F. Deng, X. Han, X. Bao, J. Phys. Chem. C **117**, 5848–5854 (2013)
21. Q. Wu, X. Hong, L. Zhu, X. Meng, S. Han, J. Zhang, X. Liu, C. Jin, F.-S. Xiao, Microporous Mesoporous Mater. **286**, 163–168 (2019)
22. X. Xiong, D. Yuan, Q. Wu, F. Chen, X. Meng, R. Lv, D. Dai, S. Maurer, R. McGuire, M. Feyen, U. Mueller, W. Zhang, T. Yokoi, X. Bao, H. Gies, B. Marler, D.E. De Vos, U. Kolb, A. Moini, F.-S. Xiao, J. Mater. Chem. A. **5**, 9076–9080 (2017)
23. S. Miyagawa, K. Miyake, Y. Hirota, N. Nishiyama, M. Miyamoto, Y. Oumi, S. Tanaka, Microporous Mesoporous Mater. **278**, 219–224 (2019)
24. H. Xu, J. Zhu, J. Qiao, X. Yu, N.-B. Sun, C. Bian, J. Li, L. Zhu, Microporous Mesoporous Mater. **312**, 110736 (2021)
25. C. Lee, S. Lee, W. Kim, R. Ryoo, Catal. Today **303**, 143–149 (2018)
26. X. Niu, J. Gao, Q. Miao, M. Dong, G. Wang, W. Fan, Z. Qin, J. Wang, Microporous Mesoporous Mater. **197**, 252–261 (2014)
27. T. Fu, J. Shao, Z. Li, Appl. Catal. B: Environ. **291**, 1298 (2021)
28. N. Wang, J. Li, W. Sun, Y. Hou, L. Zhang, X. Hu, Y. Yang, X. Chen, C. Chen, B. Chen, W. Qian, Angew. Chem. Int. Ed. (2022). https://doi.org/10.1002/anie.202114786
29. T. Sano, M. Itakura, M. Sadakane, J. Jpn. Petrol. Inst. **56**, 183–197 (2013)

30. R. Xu, W. Pang, J. Yu, Q. Huo, J. Chen, *Chemistry of zeolites and related porous materials* (Wiley, Chichester, 2007)
31. J. Devos, M.A. Shah, M. Dusselier, RSC Adv. **11**, 26188–26210 (2021)
32. P. Zhang, S. Li, P. Guo, X. Zhao, Langmuir **36**, 6160–6168 (2020)
33. P.T. Ngo, P.N.X. Vo, L.P. Trinh-Le, D.T. Pham, P.D. Phan, C.V. Cao, T.V. Tran, T.N. Luong, Q.L.M. Ha, N. Le-Phuc, Microporous Mesoporous Mater. **315**, 110928 (2021)
34. Z. Han, F. Zhang, X. Zhao, Microporous Mesoporous Mater. **290**, 109679 (2019)
35. Yu J, in: Studies in Surface Science and Catalysis, Vol. 168, eds. J. Čejka, H. van Bekkum, A. Corma and F. Schüth (Elsevier, 2007).
36. B. Bauer, H. Strathmann, F. Effenberger, Desalination **79**, 125–144 (1990)
37. L. Xu, Y. Yuan, Q. Han, L. Dong, L. Chen, X. Zhang, L. Xu, Catal. Sci. Technol. **10**, 7904–7913 (2020)
38. D.V. Bruter, V.S. Pavlov, I.I. Ivanova, Pet. Chem. **61**, 251–275 (2021)
39. Y. Jin, Q. Sun, G. Qi, C. Yang, J. Xu, F. Chen, X. Meng, F. Deng, F.S. Xiao, Angew. Chem. **52**, 9172–9175 (2013)
40. M. Choi, R. Srivastava, R. Ryoo, Chem. Commun. (2006). https://doi.org/10.1039/b612265e
41. L.-H. Chen, X.-Y. Li, G. Tian, Y. Li, J.C. Rooke, G.-S. Zhu, S.-L. Qiu, X.-Y. Yang, B.-L. Su, Angew. Chem. Int. Ed. **50**, 11156–11161 (2011)
42. Y. Ni, A. Sun, X. Wu, G. Hai, J. Hu, T. Li, G. Li, Microporous Mesoporous Mater. **143**, 435–442 (2011)
43. Y. Jia, J. Wang, K. Zhang, W. Feng, S. Liu, C. Ding, P. Liu, Microporous Mesoporous Mater. **247**, 103–115 (2017)
44. Y. Jia, J. Wang, K. Zhang, G. Chen, Y. Yang, S. Liu, C. Ding, Y. Meng, P. Liu, Powder Technol. **328**, 415–429 (2018)
45. Y. Jia, J. Wang, K. Zhang, S. Liu, G. Chen, Y. Yang, C. Ding, P. Liu, Catal. Sci. Technol. **7**, 1776–1791 (2017)
46. A.A. Rownaghi, J. Hedlund, Ind. Eng. Chem. Res. **50**, 11872–11878 (2011)
47. D.T. Bregante, D.S. Potts, O. Kwon, E.Z. Ayla, J.Z. Tan, D.W. Flaherty, Chem. Mater. **32**, 7425–7437 (2020)
48. I.C. Medeiros-Costa, E. Dib, N. Nesterenko, J.-P. Dath, J.-P. Gilson, S. Mintova, Chem. Soc. Rev. **50**, 11156–11179 (2021)
49. T. Yokoi, H. Mochizuki, S. Namba, J.N. Kondo, T. Tatsumi, J. Phys. Chem. C **119**, 15303–15315 (2015)
50. M. Yabushita, R. Osuga, A. Muramatsu, CrystEngComm **23**, 6226–6233 (2021)